

A comprehensive analysis of air-sea CO₂ flux uncertainties constructed from surface ocean data products

Daniel J. Ford ¹, Josh Blannin ^{1,a}, Jennifer Watts ¹, Andrew J. Watson ², Peter Landschützer ³, Annika Jersild ^{4,b} and Jamie D. Shutler ¹

¹ Department of Earth and Environmental Science, University of Exeter, Cornwall, TR10 9EZ, UK

² Global Systems Institute, University of Exeter, Devon, EX4 4RJ, UK

³ Flanders Marine Institute (VLIZ), Jacobsenstraat 1, 8400 Ostend, Belgium

⁴ Max Planck Institute for Meteorology, Hamburg, Germany

^a now at: Met Office, Exeter, EX1 3PB, UK

^b now at: Global Modelling and Assimilation Office (GMAO), NASA Goddard Space Flight Center, Greenbelt, MD, USA / Earth System Science Interdisciplinary Center, University of Maryland, College Park, MD, USA

Corresponding author: Daniel J. Ford (d.ford@exeter.ac.uk)

Abstract

Increasing anthropogenic CO₂ emissions to the atmosphere are partially sequestered into the global oceans through the air-sea exchange of CO₂ and its subsequent movement to depth, and this collective large-scale absorption is commonly referred to as the global ocean carbon sink. Quantifying this ocean carbon sink provides a key component for closing the global carbon budget which is used to inform and guide policy decisions. These estimates are typically accompanied by an uncertainty budget built by selecting what are perceived as critical uncertainty components based on selective experimentation. However, there is a growing realisation that these budgets are incomplete and may be underestimated, which limits their power as a constraint within global budgets. In this study, we present a methodology for quantifying spatially and temporally varying uncertainties in the air-sea CO₂ flux calculations and data that allows an exhaustive assessment of all known sources of uncertainties, including decorrelation length scales between gridded measurements, and the approach follows standard uncertainty propagation methodologies. The resulting standard uncertainties are higher than previously suggested budgets, but the components are consistent with previous work, and they identify how the significance and importance of key uncertainty components change in space and time. For an exemplar method (the UEP-FNN-U method) the work identifies that we can currently estimate the annual ocean carbon sink to an accuracy of $\pm 0.72 \text{ Pg C yr}^{-1}$ (1 standard deviation uncertainty). Due to this method having been built on established uncertainty propagation and

approaches, it appears applicable to all data-product assessments of the ocean carbon sink.

Highlights

1. A framework to calculate standard uncertainty budgets for air-sea CO₂ flux data that considers all known sources of uncertainty is described.
2. Spatially and temporally varying air-sea CO₂ flux uncertainties including their spatial decorrelation lengths are calculated.
3. For an exemplar data-product based estimate of the global ocean carbon sink we identify a 1 σ uncertainty of ± 0.72 Pg C yr⁻¹.

1. Introduction

Anthropogenic carbon dioxide (CO₂) emissions are continuing to increase and since the 1800s the ocean has acted as a natural CO₂ sink helping to slow the rise in atmospheric CO₂ and the resultant global heating. This uptake equates to ~25 % of all anthropogenic CO₂ emissions and is occurring at an increasing rate reaching ~2.9 petagrams of carbon per year (Pg C yr⁻¹; 1 Pg C = 10¹⁵ grams of carbon) in recent years (Friedlingstein et al., 2023). Our ability to quantify and resolve the annual uptake of CO₂ by the global oceans currently comes from two sources; (1) observation data-product based assessments that extrapolate and combine sparse ocean CO₂ observations with satellite and re-analysis data into global fields through time and (2) analyses from complex global biogeochemical models. Along with globally complete datasets, the data-product based assessments also rely on sparse in situ observations of the fugacity of CO₂ in seawater (fCO_{2 (sw)}) which are collated into the annual releases of the Surface Ocean CO₂ Atlas (SOCAT) (Bakker et al., 2016). In many of these data-product based approaches, these in situ data are matched to variables such as satellite, reanalysis and model-based data of sea surface temperature (SST), salinity (SSS), mixed layer depth (MLD) and chlorophyll-a (Chau et al., 2022; Gregor & Gruber, 2021; Iida et al., 2021; Landschützer et al., 2014; Watson et al., 2020), which are used to describe the physical, biological and chemically driven variability in fCO_{2 (sw)} (Shutler et al., 2024). The relationships between these variables and fCO_{2 (sw)} are then estimated within predefined provinces or biogeochemical regions (e.g., using multi linear regressions, neural network or other machine learning techniques) to allow globally complete fCO_{2 (sw)} fields through time to be produced (Chau et al., 2022; Gregor & Gruber, 2021; Iida et al., 2021; Landschützer et al., 2016; Watson et al., 2020). These complete fields are then combined with a host of data including more satellite observations, model and re-analysis datasets to calculate the air-sea CO₂ fluxes, and then integrated into global or regional annual budgets (as described within Shutler et al., 2024 and used by most of the data-product based ocean sink estimates within Friedlingstein et al., 2023; and the six methods in Fay et al., 2021).

The current uncertainty characterisation on the resulting air-sea fluxes and the integrated net sink estimates from these outputs are largely based on a single estimates that are assumed constant in space or time. For example, Landschützer et al. (2014) estimate an uncertainty of $\sim 0.53 \text{ Pg C yr}^{-1}$ for one data-product based assessment which comprised three sources of uncertainty, though dominated mainly by one empirical parameterisation used within the calculation (the gas transfer parameterisation, which was assessed to contribute to $\sim 0.4 \text{ Pg C yr}^{-1}$ of the uncertainty budget). Within the Global Carbon Budget (GCB) (Friedlingstein et al., 2023) uncertainties on all data-product ocean carbon sink assessments are estimated (as 1 standard deviation, 1σ) using literature values for a selection of uncertainty sources including the standard deviation of the seven data product ensemble in the GCB (contributing 0.3 Pg C yr^{-1}), the $\text{fCO}_2(\text{sw})$ mapping (contributing 0.2 Pg C yr^{-1} to the uncertainty budget) from Landschützer et al. (2014), the gas transfer coefficient (0.2 Pg C yr^{-1}) from Ho et al. (2011) and Wanninkhof et al. (2013), the wind speed data input (0.1 Pg C yr^{-1}) from Fay et al. (2021), the in situ $\text{fCO}_2(\text{sw})$ observation uncertainty (0.2 Pg C yr^{-1}) from Wanninkhof et al. (2013) and a land to ocean river flux adjustment (0.3 Pg C yr^{-1} which unlike the other components is the 2σ value) due to natural CO_2 outgassed due to riverine material from Regnier et al. (2022). These components are assumed spatially and temporally independent (i.e. uncorrelated), resulting in a fixed annual standard 1σ uncertainty of $\pm 0.6 \text{ Pg C yr}^{-1}$. Whilst a good first step and pragmatic solution, this approach does not systematically identify and characterise all sources of uncertainty and largely overlooks spatial correlation which is important for some variables critical in the calculation (Watson et al., 2009). Because of this, it is likely that these estimates of the uncertainties may be underestimated, whilst many will vary through both space and time dependent upon data coverage (Hauck, Nissen, et al., 2023) and environmental conditions. Furthermore, the apparent gradual divergence that has been observed between the model and data-product based assessments within the GCB assessments (Friedlingstein et al., 2022, 2023) may be, in part, driven by, or at least confused by, unconstrained or incomplete uncertainty budgets. Jersild and Landschützer (2024) provide spatially and temporally explicit uncertainties for some components of the air-sea CO_2 flux but do not systematically evaluate all known sources of uncertainty and their approach is not simply applicable to all data-products within the GCB. Clearly, a full uncertainty budget for both the model and data-product based estimates is needed to support any conclusions as to which estimate is the more credible. Similarly, a more complete standard uncertainty budget would guide where to focus efforts towards reducing these uncertainties and improving the quantification of the global ocean CO_2 sink.

These complexities identify a desire for spatially and temporally varying uncertainties where all known sources of uncertainty are systematically evaluated into a full standard uncertainty budget. Established frameworks and methods for assessing uncertainty components exist which can be used to build standard uncertainty budgets (BIPM, 2008) which were originally developed by the metrology community, but have since seen widespread application in other scientific realms including ocean

satellite remote sensing and in situ studies (e.g., Banks et al., 2020; Dong et al., 2021) and these use standard uncertainty propagation techniques (Taylor, 1997).

Within this study, we present a complete spatially and temporally varying air-sea CO₂ flux uncertainty budget which systematically assesses all known sources of uncertainty and propagates these using standard techniques (Taylor, 1997). To complement the baseline air-sea CO₂ flux uncertainty budget, we also develop an approach to estimate spatially and temporally complete fCO_{2 (sw)} uncertainties for an exemplar feed forward neural network interpolation approach, that considers multiple sources of uncertainty. We highlight how the uncertainty approach for the interpolated fields can be adapted to other data-product based approaches which use different fCO_{2 (sw)} interpolation methods. The resulting air-sea CO₂ flux uncertainties are then globally integrated to produce a global time varying uncertainty budget for the net air-sea CO₂ flux, or ocean CO₂ sink, and the dominant components within this uncertainty budget are assessed. These results are discussed in the context of the GCB global ocean CO₂ sink uncertainty estimates but the methods can also be applied regionally. The uncertainty approach for the complete air-sea CO₂ fluxes and the integrated net sink values are applicable to any data based approach.

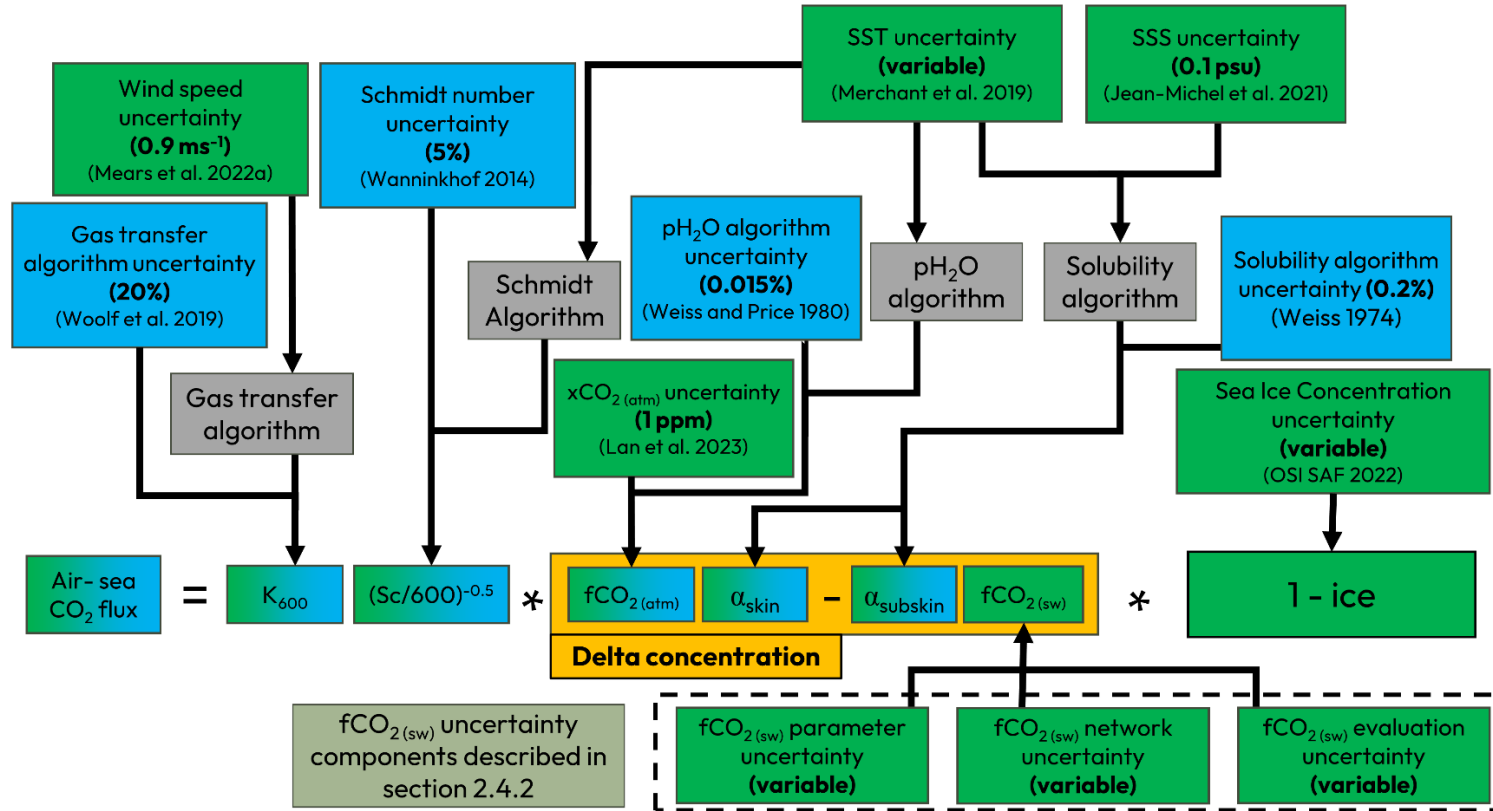


Figure 1: Flowchart indicating the sources of uncertainty that contribute to each term in the air-sea CO₂ flux calculation described in section 2.2 and integrated in section 2.5. Green boxes indicate a component that decorrelates over a spatial and temporal scale, blue boxes indicate globally correlated components and grey boxes indicate functions for which uncertainties are propagated through using a Monte Carlo approach. The fCO₂ (sw) uncertainty components (grouped by the dashed line box) are described in section 2.4.2. References within the flowchart are for the gas transfer algorithm uncertainty (Woolf et al., 2019), wind speed uncertainty (Mears et al., 2022a), Schmidt number algorithm uncertainty (Wanninkhof, 2014), partial pressure of water vapour (pH₂O) algorithm (Weiss & Price, 1980), xCO₂ (atm) uncertainty (Lan et al., 2023), SST uncertainty (Merchant et al., 2019), SSS uncertainty (Jean-Michel et al., 2021), solubility algorithm uncertainty (Weiss, 1974) and the sea ice concentration uncertainty (OSI SAF, 2022). Acronyms in flowchart are gas transfer coefficient (K_{600}), Schmidt number (Sc), fugacity of CO₂ in atmosphere ($f\text{CO}_2(\text{atm})$) and seawater ($f\text{CO}_2(\text{sw})$) and solubility at the subskin (α_{subskin}) and skin (α_{skin}).

2. Methods

2.1. Input datasets

In situ monthly 1 degree gridded SOCAT2023 fCO_2 (sw) observations which have been reanalysed to the depth consistent temperature CCI-SST v2.1 (Merchant et al., 2019) dataset were downloaded from Ford et al. (2023). Data were extracted for the period 1985 to 2022. Following the recommendations of Shutler et al. (2024) all satellite or re-analysis data choices focussed on climate data to ensure long-term data stability and the availability of uncertainty data. Satellite or reanalysis datasets were retrieved from their respective sources at their native temporal and spatial resolution (see Supplementary Table S1 for all the datasets used within this study) and averaged (mean) to the same monthly 1 degree global grid as the SOCAT observations. Some datasets did not cover the full temporal period and these periods were filled with a 10 year climatological monthly mean from the respective end of the timeseries (i.e if missing data occurred at the start of the timeseries, a 10 year monthly climatology from the start of the available data was constructed). Anomalies for each variable were calculated with respect to a monthly climatology between 1985 and 2022. The GCB (Friedlingstein et al., 2023) version of the UoEx-Watson product was retrieved from Hauck, Landschützer et al. (2023).

The CCI-SST and EUMETSAT Ocean and Sea Ice Satellite Application Facility (OSISAF) sea ice concentrations were retrieved with a daily coincident uncertainty field. The uncertainties within these data are correlated spatially to around 100-300 km and 3 days temporally (Kern, 2021), and therefore we assumed the uncertainties are correlated within these scales when producing the monthly 1 degree uncertainties.

2.2. Air-sea CO₂ fluxes

The air-sea CO₂ flux calculations were carried out using the open source FluxEngine toolbox (Holding et al., 2019; Shutler et al., 2016), which provides traceable, consistent, and configurable air-sea CO₂ flux calculations. The air-sea CO₂ flux (F) can be expressed in a bulk parameterisation as:

$$F = K_{600} (S_c / 600)^{-0.5} (\alpha_{subskin} fCO_2 (sw, subskin) - \alpha_{skin} fCO_2 (atm)) (1 - ice) \quad (1)$$

Which is consistent with the rapid model of Woolf et al., (2016) and where K_{600} is the gas transfer coefficient estimated using the Nightingale et al. (2000) parameterisation and wind speeds from the Cross Calibrated Multi-Platform dataset (CCMP; v3.1) (Mears et al., 2022a, 2022b). S_c is the Schmidt number estimated using the calculation in Wanninkhof et al. (2014) and the ocean's skin temperature. α is the solubility of CO₂ at the respective subskin or skin temperature and salinities which was estimated as in Weiss (1974). $fCO_2 (atm)$ and $fCO_2 (sw, subskin)$ are the fugacity of CO₂ in the atmosphere and the seawater subskin layer respectively. Eq. 1 and the use of skin and subskin temperatures

accounts for vertical temperature gradients across the ocean's mass boundary layer as described in Woolf et al. (2016), where we refer the reader for further information and the assignment of data to the skin and subskin quantities is described below.

For the $f\text{CO}_2(\text{sw,subskin})$, we use complete $f\text{CO}_2(\text{sw,subskin})$ fields generated by an exemplar neural network approach (University of Exeter Physics Feed Forward Neural Network with Uncertainties; UEP-FNN-U) described in section 2.4. The CCI-SST and CMEMS SSS are considered representative of the subskin temperature and salinities and used in the calculation of α_{subskin} . For the atmospheric side, the ocean's skin temperature was estimated from the CCI-SST with a cool skin deviation calculated with NOAA-COARE3.5 (Bariteau Ludovic et al., 2021; Edson et al., 2013; Fairall et al., 1996) using CCMP wind speed, CCI-SST and ERA5 fields (Hersbach et al., 2019) as inputs. Skin salinity was calculated assuming a +0.1 psu change from the CMEMS SSS (i.e a salty skin) as in Watson et al. (2020) and Woolf et al. (2019). $f\text{CO}_2(\text{atm})$ was calculated using NOAA-ERSL atmospheric dry mixing ratio of CO_2 ($x\text{CO}_2(\text{atm})$), the skin temperature and ERA5 atmospheric pressure. Sea ice concentrations from the OSISAF (OSI SAF, 2022) dataset were used for the ice component of Eq. 1.

2.3. Air-sea CO_2 flux uncertainties

The spatially and temporally varying air-sea CO_2 flux uncertainties were calculated using a framework that assesses all identified sources of uncertainties (Figure 1). Figure 1 indicates the sources of uncertainties that contribute to the individual components of Eq. 1. Uncertainties within each component were propagated through the flux calculations using standard propagation techniques (e.g., where a specific value is known) or a Monte Carlo uncertainty propagation approach (e.g., where the component is dependent upon input data), to produce an uncertainty in the air-sea CO_2 flux due to each component (considered 95% confidence).

As an example, the process for propagating the uncertainties contributing to the K_{600} uncertainty are described, where these principles apply to all components. K_{600} shows two sources of uncertainty: (1) the gas transfer parameterisation uncertainty when parameterised with in situ observations, which has been indicated as ~20% (Woolf et al., 2019) and (2) the uncertainty within the wind speed product used in driving the gas transfer parameterisation. The first component can be propagated with standard propagation techniques, resulting in a 20 % uncertainty (assumed to be 95 % confidence) in the calculated CO_2 flux. The second wind speed uncertainty component was propagated through the gas transfer parameterisation using a Monte Carlo uncertainty propagation, where the wind speed was perturbed randomly 100 times within its uncertainty (0.9 ms^{-1} where we assume this was a 95% confidence) (Mears et al., 2022a). The one standard deviation of the resulting distribution of K_{600} were calculated, converted to a percentage uncertainty, and propagated using standard propagation techniques to a CO_2 flux uncertainty. This resulted in a spatially varying uncertainty with a global

mean of ~20 %, however significantly varying regionally, ranging from 10 % to greater than 100 %. For a total uncertainty on K_{600} for each 1 degree region, the two components could be combined in quadrature assuming they are independent and uncorrelated (Taylor, 1997). This approach and principles apply to all components in Figure 1 except for the sea ice concentration and the interpolation of the fCO_2 data. The uncertainty estimate of the interpolated fCO_2 is a more specialised case which needs to capture multiple sources of uncertainty, which are the network uncertainty, input parameter uncertainties (of the inputs used for the interpolation) and the evaluation uncertainty, and the approach taken for this are given in the section 2.4.2. The sea ice uncertainty contribution was not included in the total air-sea CO_2 flux uncertainty due to the asymmetric nature of the sea ice concentration when applying a Monte Carlo uncertainty propagation (i.e the sea ice concentration cannot be less than 0 % or greater than 100 % and therefore the resulting uncertainty distribution after applying the Monte Carlo uncertainty propagation would become skewed). These asymmetric distributed uncertainties cannot be combined with the symmetric uncertainty distributions using standard propagation techniques (Taylor, 1997). Therefore the sea ice concentration uncertainties are assessed within the globally integrated uncertainties described in section 2.5.

2.4. Calculating spatially complete $fCO_{2(sw)}$ data and estimating their uncertainties

The sparse sampling of the in situ data used, the need to use an interpolation method, and the need for input data for the interpolation methods warrants a more comprehensive analysis of the fCO_2 data uncertainties. These sections now describe the interpolation technique and the approach for assessing the uncertainties for input into the framework in Figure 1.

2.4.1 The neural network approach - University of Exeter physics feed forward neural network with uncertainties (UEP-FNN-U)

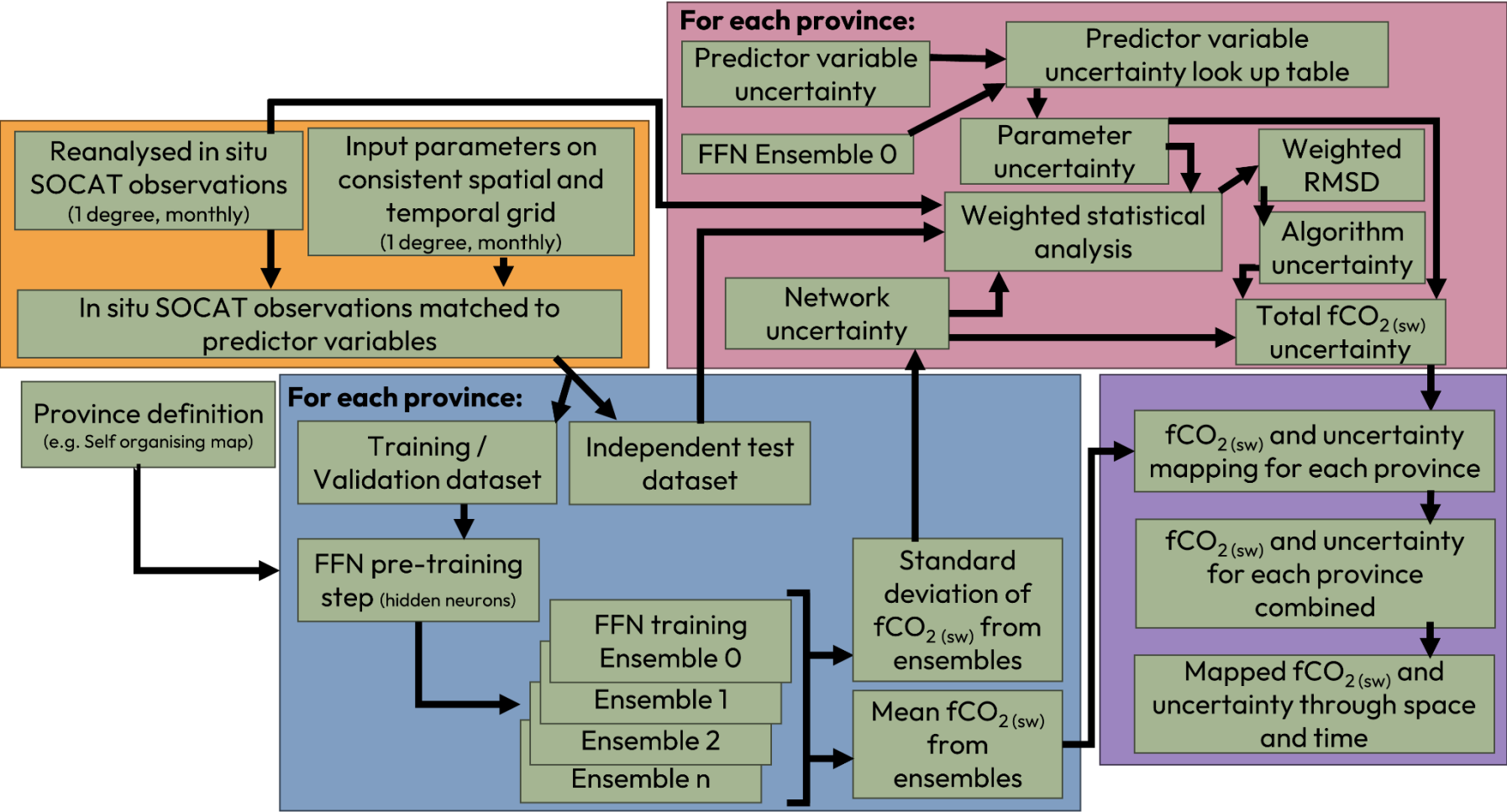
The self-organising map feed forward neural network (SOM-FNN) method (Landschützer et al., 2014, 2016) used within the GCB (Friedlingstein et al., 2023) UoEx-Watson product (Watson et al., 2020) was applied with modifications to interpolate the re-analysed SOCAT sourced in situ fCO_2 data. These modification were: the Arctic Ocean was defined as a single province using the Longhurst province (Longhurst, 1998) Boreal Arctic (Province 1). The Mediterranean Sea and Red Sea Longhurst provinces (Province 16 and 25 respectively) were combined into a single province covering these regions, leading to a total of 18 provinces (instead of 17 as in UoEx-Watson) and near global coverage. Whereas the predictor variables remained consistent to the UoEx Watson product, consisting of SST, SSS, MLD, $xCO_{2(atm)}$, and anomalies of all four variables (Table 1).

These predictor variables were matched in space and time to the re-analysed SOCAT observations (Figure 2). For each province the SOCAT gridded $fCO_{2(sw)}$ observations, with their respective

predictor variables, were split into two datasets; (1) an independent test dataset that was not used in the neural network training or validation steps (5 %) and (2) a training and validation dataset (95 %). This data split provides as much of the data to the neural network training, whilst retaining a sufficient sample to independently assess the neural network performance. The training and validation dataset was then used within a feed forward neural network (FNN). The FNN approach consists of an input layer, hidden layer, and output layer. The input layer consists of nodes corresponding to the number of predictor variables, and a single node in the output layer. The number of nodes within the hidden layer was determined through a pre-training step (Ford et al., 2022a; Landschützer et al., 2014), which incrementally increases the hidden layer nodes in a set range (30 to 300 nodes at 30 increments) and finds the minimum of the neural network loss function which corresponds to the root mean square difference (RMSD) between the neural network output and the validation component training dataset. The pre-training step was required to provide the optimum number of hidden neurons to fit the in situ observations, whilst preventing overfitting (Demuth et al., 2008). Once the optimum number of nodes in the hidden layer was selected an ensemble of 10 neural networks are trained using the training and validation dataset. The training and validation dataset was split further and randomly into the training (70 %) and validation datasets (30 %) for each ensemble member. The split percentages were estimated with the optimal split approach described in Amari et al. (1997). This random splitting allows the neural network ensemble a high probability to see all the dataset as either training or validation data. Once all ensembles have been trained, the output $f\text{CO}_2(\text{sw})$ for the province was the mean of the ensembles. Applying this ‘mean’ neural network for each province to the complete fields of the predictor variables allows the generation of complete and spatially complete $f\text{CO}_2(\text{sw})$ fields (Figure 2).

Table 1: Input parameters used within the University of Exeter physics feed forward neural network (UEP-FNN-U) as predictor variables, with their respective uncertainties used within the parameter uncertainty.

| Predictor Variables | Defined Uncertainty | Reference |
|--|----------------------------|----------------------------|
| NOAA $x\text{CO}_2(\text{atm})$ | 1 ppm | (Lan et al., 2023) |
| CCI Sea Surface Temperature (v2.1) | 0.15 K | (Merchant et al., 2019) |
| CMEMS sea surface salinity (GLORYS12) | 0.1 psu | (Jean-Michel et al., 2021) |
| CMEMS mixed layer depth (GLORYS12; \log_{10} transformed) | 0.05 $\log_{10}(\text{m})$ | (Jean-Michel et al., 2021) |



260

261 **Figure 2:** Flowchart indicating the structure and training scheme of the feed forward neural network approach and uncertainty analysis as described within
262 section 2.4.1 and 2.4.2. Acronyms in the flowchart are Surface ocean CO₂ Atlas (SOCAT), fugacity of CO₂ in seawater (fCO_{2 (sw)}), feed forward neural
263 network (FFN) and root mean square difference (RMSD).

2.4.2 Spatial and temporally varying $\text{fCO}_2(\text{sw})$ uncertainty determination

The characterisation of uncertainties in the $\text{fCO}_2(\text{sw})$ neural network approach applied here allows the determination of spatially and temporally varying uncertainties in the estimated $\text{fCO}_2(\text{sw})$. Three sources of uncertainty in the neural network $\text{fCO}_2(\text{sw})$ are considered (and shown in Figure 2 in detail) and these are analysed and then included within the air-sea CO_2 flux uncertainties framework within Figure 1 (see the three boxes that are grouped by a dashed line in the bottom right of Figure 1).

The first uncertainty component consists of the neural network uncertainty, whereby the random nature of the neural network approaches can lead to different optimum outcomes of a single network. This uncertainty was assessed as two standard deviations (2σ) of 10 neural network ensemble runs described in section 2.4.1 thereby providing the mean and standard deviation of the ensembles on a per pixel basis. Regions where the 2σ value is small, indicates where the neural networks ensembles are well constrained with different training and validation splits, and so output similar $\text{fCO}_2(\text{sw})$ estimates with low variability between estimates. The first ensemble member is also used within the second uncertainty component of the $\text{fCO}_2(\text{sw})$.

The second uncertainty component considered is the impact of the uncertainties in the predictor variables on the resulting interpolated fields, as described in Ford et al. (2021), and applied to $\text{fCO}_2(\text{sw})$ in Ford et al. (2022a). The uncertainties in the predictor variables were propagated through the first neural network ensemble (for practical reasons, this analysis was only applied to the first member of the ensemble described above due to the computational load). In summary, a n-dimensional (n being the number of predictor variables) linear spaced grid was constructed between the maximum and minimum of each predictor variable. The linear spacing was determined such that the total number of grid points does not exceed a defined value (whereby increasing this number increases the resolution of the grid but increases computation). At each point in the grid, the predictor variables were randomly perturbed within their uncertainty (Table 1; assuming these are 95% confidence) and the $\text{fCO}_2(\text{sw})$ estimated for each perturbation. The one standard deviation of the resulting $\text{fCO}_2(\text{sw})$ distribution was taken as the input parameter uncertainty. The process is repeated for every combination in the n-dimensional grid. This grid became a look-up table for the input parameter uncertainty on the $\text{fCO}_2(\text{sw})$ using linear interpolation between grid points. Thus, allowing the determination of the input parameter uncertainty at any combination of input variables, in a computationally efficient setup.

The third uncertainty component considered was the evaluation uncertainty, or how accurate and precise the neural network estimates of the $\text{fCO}_2(\text{sw})$ are with respect to the in situ gridded SOCAT observations. For each province the independent test observations are compared to the neural network ensemble mean using a weighted statistical analysis as described in Ford et al. (2021). The weighting procedure allows both uncertainties in the neural network and the in situ data to be included in the

assessment of the evaluation uncertainty. The neural network uncertainty for the weighting was determined as the network and input parameter uncertainties combined in quadrature (Taylor, 1997), consistent with Ford et al. (2021). The in situ observation uncertainty was calculated as the standard deviation of the in situ SOCAT observations in a particular grid cell combined in quadrature with an assumed measurement uncertainty of 5 μatm (Bakker et al., 2016; Taylor, 1997) (so information from the two previously described uncertainty components are used within the derivation of this third component). The weighted statistical analysis provides the bias (accuracy), root mean square difference (RMSD; precision), along with the slope and intercept of a type II linear regression and the number of observations. The neural network approaches generally have a bias (accuracy) near ~ 0 μatm indicating a high accuracy, however the RMSD (precision) is generally larger (values closer to ~ 0 indicate a higher precision) (Ford et al., 2022a; Gregor et al., 2019; Landschützer et al., 2014). For each province the weighted RMSD was taken as the combined algorithm uncertainty, and the bias assumed to be negligible (i.e. maximum biases are $\sim 10\%$ of the corresponding RMSD) compared to the RMSD (example per province scatter plots shown in Supplementary Figure S1).

Once all three components are calculated, these are combined in quadrature (Taylor, 1997) to provide the total uncertainty on the $f\text{CO}_2(\text{sw})$. The three uncertainty components are all calculated or applied during the mapping procedure to produce complete fields of $f\text{CO}_2(\text{sw})$ with a concurrent total uncertainty (considered a 95% confidence uncertainty).

2.5. Integrated air-sea CO_2 fluxes and uncertainties

The monthly air-sea CO_2 fluxes and their uncertainties can be used to construct annual global budgets of the net CO_2 flux. The area of each pixel was calculated assuming the Earth is an ellipsoid, and high resolution land percentage masks were produced from The General Bathymetric Chart of the Oceans (GEBCO) bathymetry data (GEBCO Bathymetric Compilation Group, 2023). The high resolution approach ensures that coastal region contours are well captured to avoid unnecessary precision or rounding errors (as described by Shutler et al., 2016). The calculated CO_2 fluxes ($\text{g C m}^{-2} \text{d}^{-1}$) are multiplied by the pixel area (m^2), land percentage masks, the days within each month and then summed into annual CO_2 fluxes (Pg C yr^{-1}). The annual absolute air-sea CO_2 flux was also calculated (i.e. $|F|$, the absolute air-sea CO_2 flux from Eq 1, regardless of whether into or out of the ocean).

The integration of the air-sea CO_2 flux uncertainties within the uncertainty budget must be treated carefully (Figure 1). In general most components within the air-sea CO_2 flux calculations have a systematic component that will be correlated globally (Figure 1; blue boxes) and a component that will be correlated to a spatial and temporal scale (Figure 1; green boxes). Following standard geostatistical methods these two components (correlated globally and correlated to a spatial/temporal scale) must be treated differently when integrating globally (see the Supplementary of Watson et al.,

2009). The globally correlated components (Figure 1; blue boxes) can be integrated in the same way as the air-sea CO₂ fluxes. So the CO₂ flux uncertainty ($\text{g C m}^{-2} \text{d}^{-1}$) at each pixel location was first multiplied by the area of the pixel (m^2), land percentage mask and the number of days in the month, and then summed into an annual CO₂ flux uncertainty for each systematic component (Pg C yr^{-1}). Whereas the procedure for globally integrating the uncertainty component that correlates to a spatial and temporal scale (Figure 1; green boxes) requires an understanding of the scales at which spatial features, and therefore their associated uncertainties, decorrelate. It was firstly assumed that the uncertainties are not correlated between months (i.e no temporal correlation) as previous work shows that for the SST (from the CCI-SST data) and sea ice concentrations (from the OSISAF data) the uncertainties correlate up to period of only a few days (Kern, 2021). The spatial decorrelation length for each component (Figure 1; green boxes) was assessed using a semi-variogram approach, as used in previous studies (Landschützer et al., 2013, 2014; Watson et al., 2009). The analysis calculates the semi-variance within the uncertainty field at point-to-point Haversine distances and estimates the ‘range’, or the distance at which the semi-variance does not change. The range indicates the distance within which the uncertainties can be deemed to be correlated.

The following methods are consistent with the variogram analysis used for air-sea CO₂ gas fluxes within Watson et al. (2009) and Landschützer et al. (2013, 2014). The semi-variogram analysis was implemented using SciKit-GStat v1.0 (Mälicke, 2022) parameterised with the Dowd semi-variance estimator and fit to an exponential variogram model. The semi-variogram was fit to a random subsample of 200 points extracted from each month’s uncertainty fields and repeated 100 times. The monthly perturbations were combined into an annual distribution (~1200 perturbations) and the median and interquartile range extracted from the distribution (example histograms for SST shown in Supplementary Figure S2). In cases where a monthly uncertainty field had less than 200 points, the subsample was constructed on the number of available points divided by two.

The uncertainty fields supplied to the semi variogram analysis fell into three categories: (1) a complete uncertainty field, (2) incomplete fields of the residuals between the parameter and in situ observations or (3) complete residual fields between two datasets for the parameter. The SST (CCI-SST), and sea ice concentration (OSISAF) and fCO₂(_{sw}) network uncertainty (Figure 1) had full uncertainty fields (category 1) which were applied to the semi variogram analysis indicating median decorrelation lengths of ~1300 km, ~1500 km and ~1800 km respectively between 1985 and 2022. Although complete uncertainty fields were available for fCO₂(_{sw}) parameter and evaluation, these fields have non-continuous values resulting in a lack of convergence for the semi-variogram analysis (i.e the methodological decisions in section 2.4.2 cause these fields to be roughly single values for each province). Therefore for the fCO₂(_{sw}) evaluation and parameter uncertainties, we have to use an incomplete uncertainty field (category 2 field) to estimate the decorrelation lengths. The residuals between the in situ monthly SOCAT fCO₂(_{sw}) observations and the neural network ensemble mean are

mapped (category 2) and supplied to the semi-variogram approach. This gave a median decorrelation length of ~2400 km. The wind speed uncertainty presents no complete uncertainty field or in situ observations and therefore we assess the spatial residual variability between two differing wind speed datasets, CCMP v3.1 and ERA5 wind speeds (category 3) as an estimate of the decorrelation lengths. This analysis estimated a median decorrelation lengths of ~4000 km. Finally for $x\text{CO}_2(\text{atm})$ we assign a decorrelation length of 2000 ± 1500 km estimated using the global locations of the in situ stations that supply data to the NOAA-ERSL product, and for SSS we assume the uncertainty decorrelated at the same spatial scale as the CCI-SST (~1300 km). The calculated decorrelation lengths varied in time and had their respective uncertainties.

These decorrelation lengths have previously been used to estimate the number of decorrelated areas within a region, either globally (Landschützer et al., 2014) or regionally (Landschützer et al., 2013; Watson et al., 2009). The number of decorrelated regions are then combined with a spatially fixed uncertainty to estimate the integrated uncertainty. However, in this study we have estimated spatially varying uncertainty fields which cannot be applied to the methodology of the previous studies. We therefore integrate the uncertainty component that correlates to a spatial scale using the calculated decorrelation lengths and spatially varying uncertainty fields within a Monte Carlo uncertainty propagation.

In summary, a global grid of points was calculated where each point was separated by twice the decorrelation length for the component being calculated. At each point a random value between -1 and 1 was assigned. These values were then linearly interpolated onto the same 1 degree global grid as the air-sea CO_2 flux data, such that each global 1 degree location has a value between -1 and 1 assigned. This was repeated for each month in the timeseries between 1985 and 2022 producing a global grid of perturbation values through time. This perturbation grid has systematic spatial structures (of values between -1 and 1) that are consistent with the decorrelation length scale, and therefore the number of decorrelated areas in previous studies (Landschützer et al., 2014; Watson et al., 2009). The complete space time fields of the air-sea CO_2 flux uncertainty were multiplied by the perturbation values and added to the calculated air-sea CO_2 flux. The annual net CO_2 flux budget calculations described at the start of section 2.5 were conducted on the perturbed air-sea CO_2 fluxes. This process was repeated 100 times with the decorrelation length perturbed randomly within its uncertainty at the start of each ensemble. The two standard deviations of the resulting 100 ensembles of annual net CO_2 fluxes were taken as the globally integrated uncertainty of the component.

To provide confidence in our Monte Carlo uncertainty propagation methodology we replicate the global integrated $f\text{CO}_2(\text{sw})$ uncertainty presented in Landschützer et al. (2014) of $\sim 0.18 \text{ Pg C yr}^{-1}$ (1σ) for the period 1998 to 2010. Here we supply the calculated decorrelation lengths for the $f\text{CO}_2(\text{sw})$ evaluation uncertainty in this study, as our neural network approach is based on the Landschützer et

al. (2014) methodology, and a fixed $f\text{CO}_2(\text{sw})$ evaluation uncertainty of 12 μatm . With these inputs the Monte Carlo uncertainty propagation estimates a 1σ uncertainty of $\sim 0.17 \text{ Pg C yr}^{-1}$ for the period 1998 to 2010, which is within 6% of, and consistent with, the Landschützer et al. (2014) result.

The integrated uncertainty components were calculated at the 95% confidence (or equivalent to a 2 sigma uncertainty), but to enable comparisons to the GCB values (Friedlingstein et al., 2023) we also express these at 1 sigma.

3. Results

3.1. $f\text{CO}_2(\text{sw})$ and $f\text{CO}_2(\text{sw})$ uncertainties

The UEP-FNN-U estimated mean $f\text{CO}_2(\text{sw})$ between 1985 and 2022 showed global spatial variability consistent to the UoEx-Watson data product, but with extended coverage into the Arctic ocean and Mediterranean Sea (Supplementary Figure S3; Figure 3a). The concurrent mean total $f\text{CO}_2(\text{sw})$ uncertainty estimated from the neural network showed a mean value of $\sim 30 \mu\text{atm}$, with clear geographical differences (Figure 3b). The subtropics generally showed lower uncertainties around $\sim 20 \mu\text{atm}$, whereas larger uncertainties were prevalent in the Arctic Ocean, Southern Ocean and Equatorial Pacific with values greater than $40 \mu\text{atm}$.

The dominant component driving the total $f\text{CO}_2(\text{sw})$ uncertainty varied spatially (Figure 3 c,d,e). The $f\text{CO}_2(\text{sw})$ parameter uncertainty showed consistently lower values ranging from $2 \mu\text{atm}$ up to maxima at $\sim 10 \mu\text{atm}$ (Figure 3d). Maxima generally occurred in dynamic regions including the Arctic and Equatorial Pacific, however the parameter uncertainty was not a dominant source to the total uncertainty. The network uncertainty indicated minima around $\sim 10 \mu\text{atm}$ which occurred in the subtropics and increased to maxima greater than $\sim 50 \mu\text{atm}$ in the Arctic Ocean (Figure 3c). The evaluation uncertainty ranged from $\sim 10 \mu\text{atm}$ in the subtropics and Mediterranean Sea, up to maxima $\sim 40 \mu\text{atm}$ in the polar North Atlantic Ocean (Figure 3e). The evaluation uncertainty was generally the dominant component in the subtropics and the polar North Atlantic, whereas the network uncertainty was the dominant component in the Arctic Ocean and Equatorial Pacific. The network and evaluation uncertainties were both important components within the Southern Ocean (Figure 3c, e).

3.2. Air-sea CO_2 flux uncertainties

The mean total air-sea CO_2 flux uncertainties between 1985 and 2022 showed minima around $\sim 0.01 \text{ g C m}^{-2} \text{ d}^{-1}$ in the subtropics to maxima greater than $0.1 \text{ g C m}^{-2} \text{ d}^{-1}$ in the polar oceans (Figure 4a). In all regions, the total $f\text{CO}_2(\text{sw})$ uncertainty was the dominant component, with relative contributions ranging from 50 % to 75 % (Figure 4 b,c,d,e; Bar 0). In most regions, the next largest components to the uncertainty generally stemmed from the gas transfer parameterisation and the wind speed

uncertainties which is the dominant input to the gas transfer calculation (Figure 4 b,c,d,e; Bar 1). In the Southern Ocean, the gas transfer parameterisation uncertainty was larger with relative contributions greater than 50 %, compared to the wind speed uncertainty (Figure 4e; Bar 2). In the polar North Atlantic, the gas transfer parameterisation and wind speed both contributed the same (Figure 4c; Bar 2). However, in the subtropical South Atlantic and Equatorial Pacific the wind speed uncertainty was larger than the gas transfer parameterisation component (Figure 4 a,d; Bar 2). The remaining uncertainty components, including the $f\text{CO}_2(\text{atm})$, air and waterside solubilities and Schmidt number, were generally smaller components with relative contributions totalling to around 5 % of the total uncertainty (Figure 4 b,c,d; Bar 0). However in the Southern Ocean, the air and waterside solubility components accounted for ~20 % of the total uncertainty and were larger than the gas transfer and wind components (Figure 4e; Bar 0).

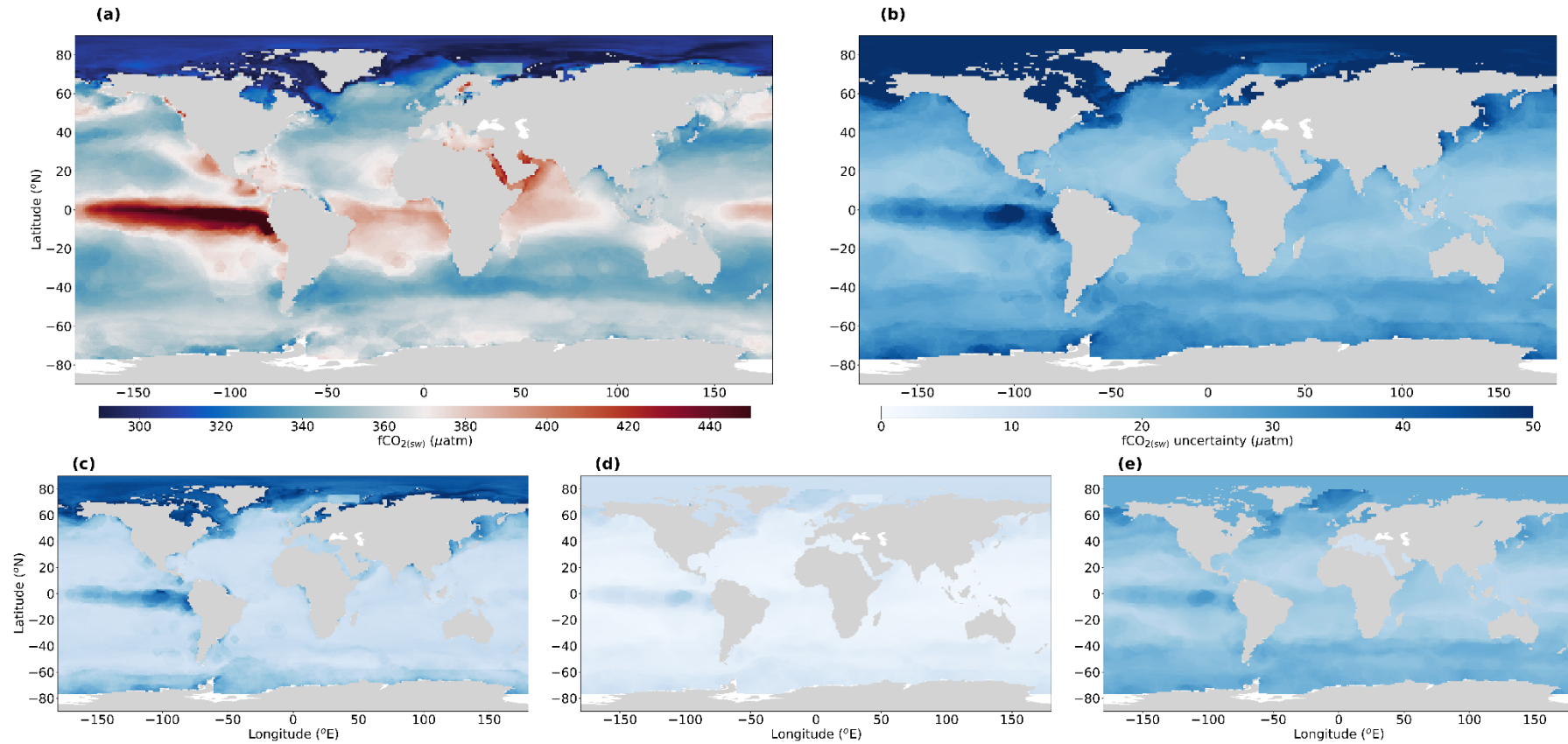
3.3. Integrated net air-sea CO_2 flux and uncertainties

The globally integrated net air-sea CO_2 flux indicated a net CO_2 sink of ~2.2 Pg C yr^{-1} between 1985 to 1995 before reducing to a minimum in 2000 of ~2.0 Pg C yr^{-1} . There after the CO_2 sink increased steadily from ~2.0 Pg C yr^{-1} in 2002 to ~3.4 Pg C yr^{-1} in 2020 (Figure 5d). The evolution of the CO_2 sink estimated by the UEP-FNN-U was consistent with that of the UoEx-Watson product (Figure 5d). The one sigma total integrated CO_2 flux uncertainty had a mean of ~0.72 Pg C yr^{-1} between 1985 and 2022, ranging from a minimum of ~0.60 Pg C yr^{-1} around 2000 to a maximum of ~0.85 Pg C yr^{-1} in 2021 (Figure 5d; Table 2).

The dominant components contributing to the total uncertainty changed over the period 1985 to 2022 (Figure 5a). Between 1985 and 2000, the $f\text{CO}_2(\text{sw})$ uncertainty decreased from ~0.65 Pg C yr^{-1} to ~0.45 Pg C yr^{-1} but remained the dominant component in this period. During the period 2001 to 2022, the $f\text{CO}_2(\text{sw})$ and gas transfer uncertainties show relatively equal contributions to the total uncertainty of ~0.49 Pg C yr^{-1} . However after ~2010 the gas transfer uncertainties were marginally more dominant. The $f\text{CO}_2(\text{sw})$ uncertainty was made up by the three sources of neural network uncertainty (Figure 5b). The parameter uncertainty showed the lowest contribution of ~10 %, whereas the evaluation and network uncertainties have contributions of 50 % and 40 % respectively. But these contributions changed through time, whereby the evaluation uncertainty contribution were generally higher at the start and end of the timeseries, with minima around 1997. The network uncertainty showed a reciprocal change to that of the evaluation uncertainty, whereas the parameter uncertainty stayed relatively constant through time.

The gas transfer parameterisation uncertainty was the next dominant component of uncertainty after the $f\text{CO}_2(\text{sw})$, increasing from 0.40 Pg C yr^{-1} in 1985 to 0.58 Pg C yr^{-1} in 2022. This increase largely followed the increase in the absolute air-sea CO_2 flux, from 4 Pg C yr^{-1} in 1985 to 5.8 Pg C yr^{-1} in

2022 (Figure 5d). After ~2010 the gas transfer parameterisation became the marginally more dominant source of uncertainty, and before this period the $f\text{CO}_{2(\text{sw})}$ remained the dominant source of uncertainty. The other components showed lower contributions to the total uncertainty with mean contributions between 1985 and 2022 of $0.14 \text{ Pg C yr}^{-1}$ for the wind speed, $0.08 \text{ Pg C yr}^{-1}$ for the solubility components, $0.06 \text{ Pg C yr}^{-1}$ for the Schmidt number, $0.02 \text{ Pg C yr}^{-1}$ for the $f\text{CO}_{2(\text{atm})}$ and $0.003 \text{ Pg C yr}^{-1}$ for the sea ice uncertainty. The $f\text{CO}_{2(\text{atm})}$ component was dominated by the $x\text{CO}_{2(\text{atm})}$ uncertainty and contained a 25 % relative contribution from the partial pressure of water vapour (pH_2O) component used in the calculation (Figure 5c). These components showed small increases following the increase in the absolute air-sea CO_2 flux (Figure 5d).



483

484 **Figure 3:** (a) Global mean fCO₂(sw) between 1985 and 2022 where the colorbar is centred on the mean atmospheric CO₂ concentration for the same period. (b)
 485 Global mean total fCO₂(sw) uncertainty between 1985 and 2022. (c) same as (b) but for the fCO₂(sw) network uncertainty. (d) same as (b) but for the fCO₂(sw)
 486 parameter uncertainty. (e) same as (b) but for the fCO₂(sw) evaluation uncertainty. Note (c), (d) and (e) are plotted on the same colorbar as (b).

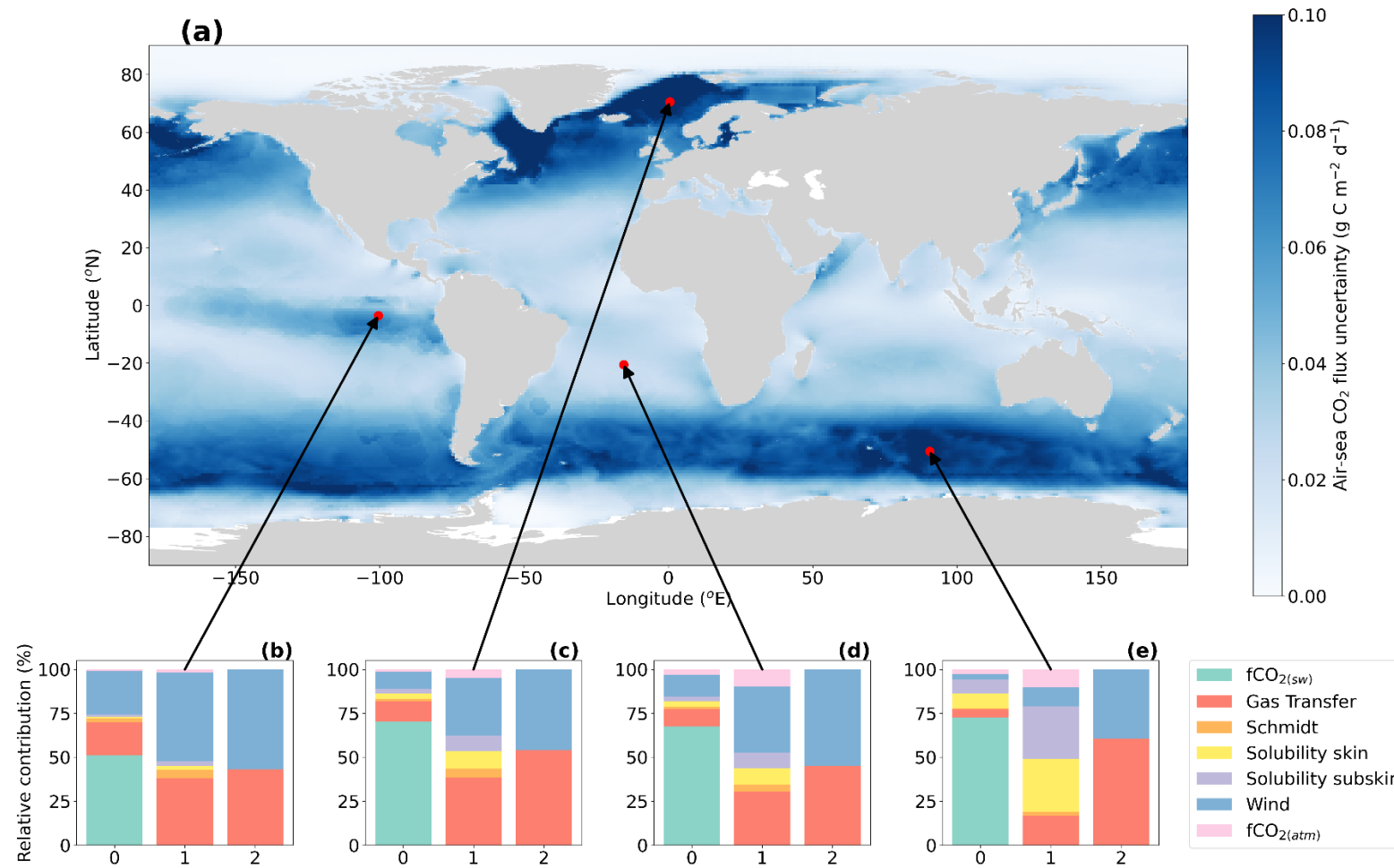


Figure 4: (a) Global mean air-sea CO₂ flux uncertainty between 1985 and 2022. (b) Mean relative contribution bar chart for each of the air-sea CO₂ flux uncertainty components between 1985 and 2022 at the highlighted location. Bar 0 shows all labelled sources of uncertainty. Bar 1 shows the contributions for all components removing the fCO_{2(sw)} component. Bar 2 shows the relative contribution for the wind speed and gas transfer components. (c), (d) and (e) same as (b) but for the respective points highlighted.

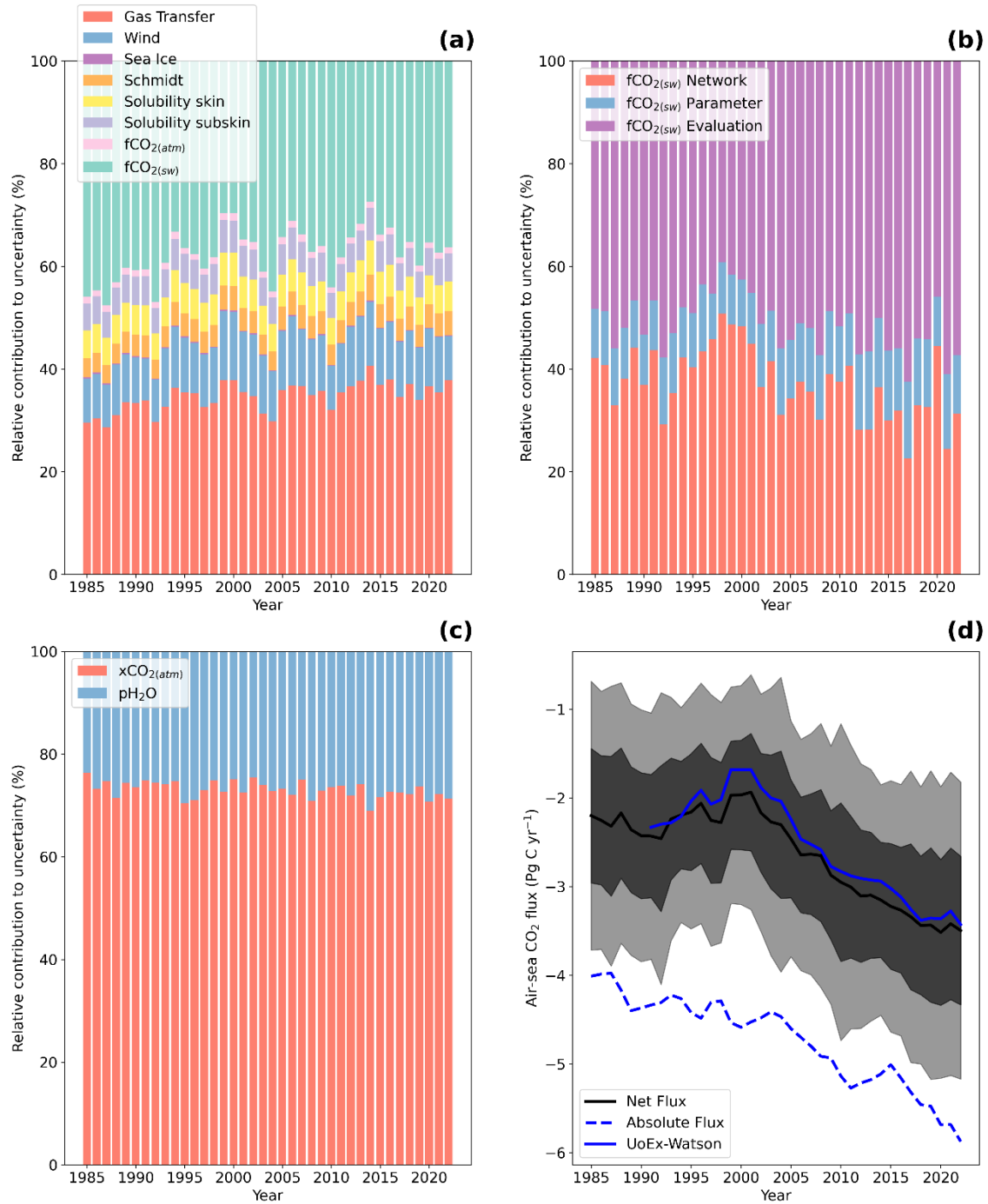


Figure 5: (a) Mean relative contributions between 1985 to 2022 for each uncertainty component to the globally integrated air-sea CO₂ flux. (b) Same as (a) but for the three fCO_{2(sw)} uncertainty components that contribute to the total fCO_{2(sw)} in (a). (c) same as (b) but for the two uncertainty components that contribute to the fCO_{2(atm)} in (a). (d) Net air-sea CO₂ flux calculated between 1985 and 2022 (black line). Dark grey region indicates the one sigma, and light grey region indicates the two sigma total air-sea CO₂ flux uncertainty. Blue dashed line indicates the absolute air-sea CO₂ flux (i.e the integrated absolute CO₂ flux across the air-sea interface). Blue line indicates the UoEx-Watson product from the Global Carbon Budget 2023 (Friedlingstein et al., 2023).

Table 2: Mean 1σ uncertainty between 1985 to 2022 for each component. These mean uncertainty can be split into a fixed (globally correlated) component and a component that was correlated to a spatial and temporal period. The total mean uncertainty between 1985 and 2022 assuming the uncertainties are independent and uncorrelated (Taylor, 1997) is shown in the total row. Equivalent 2σ uncertainties shown in Supplementary Table S2.

| Component | Mean 1σ uncertainty between 1985 to 2022 (Pg C yr ⁻¹) | Mean fixed component contribution (Pg C yr ⁻¹) | Mean spatially varying component (Pg C yr ⁻¹) |
|------------------------|--|--|---|
| Gas transfer | 0.47 | 0.47 | N/A |
| Wind | 0.14 | N/A | 0.14 |
| Sea ice | 0.003 | N/A | 0.003 |
| Schmidt | 0.06 | 0.06 | 0.001 |
| Solubility skin | 0.08 | 0.08 | 0.02 |
| Solubility subskin | 0.07 | 0.07 | 0.02 |
| fCO ₂ (atm) | 0.02 | 0.005 | 0.02 |
| fCO ₂ (sw) | 0.51 | N/A | 0.51 |
| Total | 0.72 | | |

4. Discussion

4.1. Air-sea CO₂ flux and fCO₂ (sw) uncertainties

Within this study, we present an air-sea CO₂ flux uncertainty budget that builds on the principles of in situ Fiducial Reference Measurement (Banks et al., 2020) where all known sources of uncertainty are systematically considered (however small) and propagated to the final uncertainty using standard propagation techniques and a well-established uncertainty framework (BIPM, 2008; Taylor, 1997). Applying this approach has allowed the production of spatially and temporally complete air-sea CO₂ flux uncertainties. We showed in all cases that the fCO₂ (sw) uncertainties were the dominant source of uncertainty to the air-sea CO₂ flux when investigating individual locations and time points. This would indicate that when assessing variability or trends in the air-sea CO₂ fluxes, as a first step the fCO₂ (sw) uncertainty should be accounted for within these assessments. For example, Ford et al. (2022b) calculated trends in the air-sea CO₂ fluxes in the South Atlantic Ocean and showed significant trends whilst accounting for the fCO₂ (sw) and gas transfer uncertainties. However, in this study in the South Atlantic Ocean the wind speed uncertainty component was larger than the gas transfer uncertainty (Figure 4e), consistent with the results of Jersild and Landschützer (2024). Similarly in the Southern Ocean, the air and waterside solubility component were larger than both the gas transfer and wind speed uncertainties (Figure 4e). Therefore, it is important to assess all sources of uncertainties within the air-sea CO₂ fluxes as some components may be more dominant in some regions as opposed

to others (Figure 4). These uncertainties should also be considered when assessing trends and/or more complex decompositions of seasonal, interannual and decadal variability (Ford et al., 2022b; Landschützer et al., 2016, 2018). A concerted effort to implement these full uncertainty budgets for the air-sea CO₂ fluxes in preparation for future advances and reductions of uncertainties in the air-sea CO₂ flux calculations would appear critical.

Within this air-sea CO₂ flux uncertainty budget, a spatially and temporally explicit approach to estimating the total fCO_{2(sw)} uncertainty from an exemplar feed forward neural network approach (Landschützer et al., 2014; Watson et al., 2020) was implemented (named UEP-FNN-U). Previous fCO_{2(sw)} uncertainty estimates have assumed a fixed global value based on a comparison to the in situ SOCAT observations (Landschützer et al., 2013, 2014) which is equivalent to the evaluation uncertainty in this study. Our results show that in the subtropics the use of the single fixed evaluation uncertainty may be applicable, as this was the dominant uncertainty within these regions. However, within more dynamic regions, such as the Arctic Ocean and Equatorial Pacific, the evaluation uncertainty will likely underestimate the total uncertainty due to the dominance of the network uncertainty within these regions. Some regional approaches have started to incorporate these further sources of uncertainty into their total fCO_{2(sw)} uncertainty (Ford et al., 2022a). Therefore, these results would indicate a need to expand the current uncertainty estimation for globally resolved fCO_{2(sw)}, using the approach in this study as a framework.

Within the GCB multiple data-products produce globally complete fCO_{2(sw)} fields, which use different interpolation methodologies (Friedlingstein et al., 2023). These methods include neural networks (Chau et al., 2022; Landschützer et al., 2014; Watson et al., 2020), multi-linear regression (Iida et al., 2021) or other machine learning techniques (Gloege et al., 2022), and therefore the basis of the three uncertainty components to the fCO_{2(sw)} in this study can be adapted to equivalent uncertainties for these methodologies. For example, for a method that uses multi-linear regression e.g. (Iida et al., 2021) instead of a feed-forward neural network, the calculation of the evaluation uncertainty (i.e. comparison to the in situ SOCAT observations) would remain the same. The network uncertainty could be formed from either the standard deviation of multiple ensemble runs of the multi-linear regression (similar to the network uncertainty in this study) or could be constructed from the uncertainty in the linear regression fit parameters as the source of uncertainty. The parameter uncertainty would be similar to the approach in this study and would involve a Monte Carlo uncertainty propagation which propagates the input parameter uncertainties through the multi-linear regression. It is therefore clear that these uncertainties could be equivalently mapped by data-products to produce spatially and temporally complete fCO_{2(sw)} uncertainty fields in future releases. This would be important as clearly the complete fCO_{2(sw)} uncertainty fields form a key component in calculating spatially and temporally complete air-sea CO₂ flux.

4.2. Integrated air-sea CO₂ flux uncertainties

Within the GCB the ocean carbon sink has been assessed by annually integrating the calculated air-sea CO₂ fluxes. The uncertainty on these estimates is assessed using literature values, and not all sources of uncertainty are evaluated within the assessment. In this study we have systematically assessed the components that contribute to the total air-sea CO₂ flux uncertainty and showed that these vary through time (Figure 5a, d). In this section we discuss the uncertainty estimates for the different components and compare these to the current GCB uncertainty estimate.

The GCB estimate for the fCO₂(_{sw}) mapping uncertainty is 0.20 Pg C yr⁻¹, compared to the 0.51 Pg C yr⁻¹ (Table 2) uncertainty identified in this study. The GCB estimate stems from Landschützer et al. (2014) where the uncertainty was estimated using the evaluation uncertainty of ~12 µatm. As an example, applying a 12 µatm evaluation uncertainty, and assuming the network and parameter uncertainties are 0, our methodology produces a mean 0.17 Pg C yr⁻¹ uncertainty due to the fCO₂(_{sw}) between 1998 and 2010 (same period as Landschützer et al., 2014) so our calculation methods are consistent with that of the earlier Landschützer et al. (2014) work. Since the initial work by Landschützer et al. (2014), the evaluation uncertainty for most data products has increased to around ~20 µatm (22 µatm for the UEP-FNN-U; Supplementary Figure S3c) (Gregor et al., 2019). This increase in the evaluation uncertainty increases the fCO₂(_{sw}) evaluation uncertainty to a mean of 0.41 Pg C yr⁻¹ between 1985 and 2022, but within this study we also consider the network (0.29 Pg C yr⁻¹) and parameter uncertainties (0.09 Pg C yr⁻¹). These three components all contribute to the larger uncertainty of 0.51 Pg C yr⁻¹ than that estimated by Landschützer et al. (2014).

The gas transfer uncertainty has been assessed at 0.20 Pg C yr⁻¹ within the GCB, compared to the 0.47 Pg C yr⁻¹ (Table 2) in this study. Woolf et al. (2019) suggest two representative values for the gas transfer uncertainty of 0.20 Pg C yr⁻¹ (1 sigma assuming a 10 % gas transfer uncertainty) or 0.40 Pg C yr⁻¹ (1 sigma assuming a 20 % gas transfer uncertainty). In this study we estimate a slightly higher uncertainty than suggested by Woolf et al. (2019), however our results indicate that this uncertainty was proportional to the absolute air-sea CO₂ flux (Figure 5d) which is feasible given the potential bias introduced by bubbles and increasing atmospheric CO₂ concentrations (Leighton et al., 2018).

Although our result was higher than the current GCB estimate it remains consistent if the 10 % gas transfer uncertainty were selected. However, we propose the use of the 20 % uncertainty as a conservative estimate for the gas transfer uncertainty, and that this component be calculated for each product based on the absolute air-sea CO₂ flux.

Recently the evaluation of wind speed products has indicated that a 0.09 Pg C yr⁻¹ (Fay et al., 2021; Roobaert et al., 2018) uncertainty stems from the wind speed uncertainty. We have shown a slightly

larger but still consistent value of $0.14 \text{ Pg C yr}^{-1}$ (Table 2) using a different methodology. Fay et al. (2021) estimate the uncertainty as the standard deviation of the net CO_2 sink calculated using three different wind products, where the standard deviation may not, with a small sample size, represent the full uncertainty within the wind products. Our results may also be slightly larger due to the connection to the absolute air-sea CO_2 flux, which is likely different from the products used within the previous work.

The other components assessed in this study have not previously been investigated and are currently not included within the GCB estimates. The solubility components within this study introduce a $0.08 \text{ Pg C yr}^{-1}$ uncertainty. The inclusion of two solubility terms within this study stems from the inclusion of vertical temperature gradients at the ocean's surface, as described in Woolf et al. (2016). The skin and subskin solubilities are calculated at slightly different temperatures and salinities (cool and salty skin), and therefore have subtly different values when integrated globally. Within the GCB, all the data-product based assessments, except for the UoEx-Watson, do not include the vertical temperature gradients (Friedlingstein et al., 2023) and therefore have a single solubility term. Although the evidence is growing for the inclusion of these temperature gradients (Bellenger et al., 2023; Dong et al., 2022; Shutler et al., 2020; Watson et al., 2020; Woolf et al., 2016), the use of a single or two solubilities does not have a large effect on the uncertainty (i.e. $0.10 \text{ Pg C yr}^{-1}$ for two solubilities, or $0.08 \text{ Pg C yr}^{-1}$ for one solubility assuming the solubilities are independent and uncorrelated).

The sea ice component presents a very small uncertainty on the global scale of $0.003 \text{ Pg C yr}^{-1}$. The inclusion of sea ice within the air-sea CO_2 flux calculation assumes the flux decreases linearly within increasing sea ice concentration (i.e. ice is a complete barrier to air-sea fluxes) (Arrigo & Van Dijken, 2007; Shutler et al., 2016; Takahashi et al., 2009). Although there remains debate within sea ice communities as to the relationship between sea ice coverage and air-sea CO_2 fluxes. This is in part due conflicting observations that fluxes can occur through sea ice (e.g. Geilfus et al., 2014) and whether sea ice inhibits (e.g. Prytherch & Yelland, 2021) or enhances (e.g. Kohout & Meylan, 2008) turbulence, thereby modifying the CO_2 flux (see discussion and references within Watts et al., 2022). These components will introduce further uncertainties into the sea ice component but cannot currently be quantified. However, at the global scale these uncertainties will remain small relative to the other components due to the small areal coverage but will likely increase on regional scales.

We have focussed our uncertainty analysis on the global scale, however the principles and calculations applied globally are applicable to the regional scale. Within regional assessments the fixed components will remain of similar relative magnitudes. However, the spatially correlated components will increase in magnitude due to the calculated decorrelation lengths (i.e. as the region assessed gets smaller, the uncertainties within the region become more correlated and therefore larger when integrated). Previous GCB assessments have shown global agreement between the data-product

based approaches within the uncertainties (Friedlingstein et al., 2022, 2023) but regional differences are still relatively large e.g. (Fay & McKinley, 2021; Ford et al., 2022a; Friedlingstein et al., 2023). In future work, the application of the uncertainty framework in this study to regional air-sea CO₂ flux budgets will be an important step to improve future regional air-sea CO₂ flux budgets.

4.3. Uncertainty estimates for the Global Carbon Budget

The GCB has identified that the data-products and models which assess the global ocean carbon sink have been slowly diverging, and are starting to diverge outside the current calculated uncertainty (see Figure 10 in Friedlingstein et al., 2023). Hauck, Nissen et al. (2023) indicated the ocean carbon sink uncertainty for the data products may be underestimated and suggested a value of 0.6 Pg C yr⁻¹ before the riverine adjustment uncertainty was included. Within this study we show an updated mean uncertainty of 0.72 Pg C yr⁻¹ between 1985 and 2022, before the riverine adjustment and in situ fCO₂_(sw) uncertainty were included. When the in situ fCO₂_(sw) uncertainty of 0.2 Pg C yr⁻¹ (which can be calculated within the approach assuming a 2 µatm fCO₂_(sw) uncertainty that is correlated globally; (Bakker et al., 2016)) and river flux adjustment uncertainty of 0.15 Pg C yr⁻¹ (0.3 Pg C yr⁻¹ is the 2 sigma equivalent uncertainty (Regnier et al., 2022)) are included, assuming these are independent and uncorrelated we estimate a GCB equivalent mean uncertainty for the UEP-FNN-U of 0.76 Pg C yr⁻¹. Although we have calculated a fixed value here which could be used within future GCB assessments, we strongly recommend that each data product be assessed to determine their own uncertainty budgets and then a full and temporally varying uncertainty budget for the GCB data-product ensemble can be derived. Our results have shown that the size and dominance of the different components vary through time, and some components show variability that follows the absolute air-sea CO₂ flux which will be different for each product and will likely track atmospheric emissions. This study could be used as a framework to allow these uncertainties to be calculated for each data product for future releases of the GCB assessments. All software for the analysis framework and the gas flux calculations are available as open-source (CC-BY licence) and these are version controlled and fully traceable (Ford et al., 2024).

5. Conclusions

In this study, we have presented a framework to estimate spatially and temporally varying air-sea CO₂ flux uncertainties, which systematically assessed all sources of uncertainties and was built upon standard uncertainty propagation methodologies and an established uncertainty approach. We show when investigating single locations the fCO₂_(sw) was the dominant source of uncertainty to the air-sea CO₂ fluxes. However, we show the relative contributions by the remaining sources of uncertainty

varied spatially, such that the gas transfer uncertainty was not always the second most dominant source of uncertainty. The $f\text{CO}_2(\text{sw})$ uncertainties were estimated using a similar systematic uncertainty budget that considered three sources of uncertainties in an exemplar feed forward neural network scheme (the UEP-FNN-U). We show that the evaluation uncertainty (comparison to SOCAT in situ observations) was the largest source of uncertainty in the subtropics, however the network uncertainty (uncertainty within the neural network ensemble) was dominant in dynamic regions such as the Arctic Ocean. The parameter uncertainty (propagated input parameter uncertainties through the neural network) was a small contribution to the combined uncertainty.

The calculated air-sea CO_2 fluxes were integrated into an annual estimates of the net air-sea CO_2 flux, or the ocean carbon sink, between 1985 to 2022 as commonly produced for the Global Carbon Budget assessments. We present an approach to integrate the calculated air-sea CO_2 flux uncertainties providing temporally varying ocean carbon sink uncertainties. We showed a mean 1 sigma ocean carbon sink uncertainty between 1985 and 2022 of $0.72 \text{ Pg C yr}^{-1}$. Over this period, the $f\text{CO}_2(\text{sw})$ component equated to a mean of $0.51 \text{ Pg C yr}^{-1}$, followed by the gas transfer at $0.47 \text{ Pg C yr}^{-1}$. The dominant component switched from the $f\text{CO}_2(\text{sw})$ before ~ 2010 , to the gas transfer after ~ 2010 . Smaller sources of uncertainty included the wind speed uncertainty ($0.14 \text{ Pg C yr}^{-1}$), solubility ($0.08 \text{ Pg C yr}^{-1}$) and Schmidt number ($0.06 \text{ Pg C yr}^{-1}$).

Finally we provide a Global Carbon Budget equivalent mean 1 sigma uncertainty (i.e including the riverine flux adjustment and in situ $f\text{CO}_2(\text{sw})$ uncertainties) of $0.76 \text{ Pg C yr}^{-1}$ for the UEP-FNN-U. This study provides an approach to estimating a complete air-sea CO_2 flux uncertainty budget, that could be used by the community to provide time varying and consistent uncertainties for use within the Global Carbon Budget and other assessment studies.

Contributions (CRedit)

Daniel J. Ford: Conceptualization, Formal Analysis, Investigation, Methodology, Software, Validation, Visualization, Writing-original draft

Josh Blannin: Methodology, Software, Writing-review and editing.

Jennifer Watts: Conceptualisation, Writing-review and editing

Andrew Watson: Conceptualisation, Writing-review and editing, Project Administration, Funding acquisition

Peter Landschützer: Conceptualisation, Software, Writing-review and editing

Annika Jersild: Conceptualisation, Writing-review and editing

Jamie D. Shutler: Conceptualisation, Formal Analysis, Methodology, Writing-review and editing,
Project Administration, Funding acquisition, Supervision

Open research statement

Input datasets used within this study are tabulated in Supplementary Table S1 with their respective DOIs. The software used within this study is available open source at Ford et al. (2024), and updated at <https://github.com/JamieLab/OceanICU>. Output from the analysis in this study, including the input datasets on the 1 degree monthly grid, output from the UEP-FNN-U, air-sea CO₂ fluxes and their respective uncertainty components can be downloaded from Ford et al. (in prep for Zenodo).

Acknowledgements

This work was funded by the Convex Seascape Survey (<https://convexseascapesurvey.com/>) and the European Union under grant agreement no. 101083922 (OceanICU; <https://ocean-icu.eu/>) and UK Research and Innovation (UKRI) under the UK government's Horizon Europe funding guarantee [grant number 10054454, 10063673, 10064020, 10059241, 10079684, 10059012, 10048179]. The views, opinions and practices used to produce this dataset/software are however those of the author(s) only and do not necessarily reflect those of the European Union or European Research Executive Agency. Neither the European Union nor the granting authority can be held responsible for them.

The Surface Ocean CO₂ Atlas (SOCAT) is an international effort, endorsed by the International Ocean Carbon Coordination Project (IOCCP), the Surface Ocean Lower Atmosphere Study (SOLAS) and the Integrated Marine Biosphere Research (IMBeR) program, to deliver a uniformly quality-controlled surface ocean CO₂ database. The many researchers and funding agencies responsible for the collection of data and quality control are thanked for their contributions to SOCAT.

References

- Amari, S. I., Murata, N., Müller, K. R., Finke, M., & Yang, H. H. (1997). Asymptotic statistical theory of overtraining and cross-validation. *IEEE Transactions on Neural Networks*, 8(5), 985–996.
<https://doi.org/10.1109/72.623200>
- Arrigo, K. R., & Van Dijken, G. L. (2007). Interannual variation in air-sea CO₂ flux in the Ross Sea, Antarctica: A model analysis. *Journal of Geophysical Research: Oceans*, 112(C3), 2006JC003492. <https://doi.org/10.1029/2006JC003492>

- Bakker, D. C. E., Pfeil, B., Landa, C. S., Metzl, N., O'Brien, K. M., Olsen, A., et al. (2016). A multi-decade record of high-quality fCO₂ data in version 3 of the Surface Ocean CO₂ Atlas (SOCAT). *Earth System Science Data*, 8(2), 383–413. <https://doi.org/10.5194/essd-8-383-2016>
- Banks, A. C., Vendt, R., Alikas, K., Bialek, A., Kuusk, J., Lerebourg, C., et al. (2020). Fiducial reference measurements for satellite ocean colour (FRM4SOC). *Remote Sensing*, 12(8). <https://doi.org/10.3390/RS12081322>
- Bariteau Ludovic, Blomquist Byron, Fairall Christopher, Thompson Elizabeth, Jim, E., & Pincus Robert. (2021, July 16). Python implementation of the COARE 3.5 Bulk Air-Sea Flux algorithm (Version v1.1). Zenodo. <https://doi.org/10.5281/ZENODO.5110991>
- Bellenger, H., Bopp, L., Ethé, C., Ho, D., Duvel, J. P., Flavoni, S., et al. (2023). Sensitivity of the Global Ocean Carbon Sink to the Ocean Skin in a Climate Model. *Journal of Geophysical Research: Oceans*, 128(7), e2022JC019479. <https://doi.org/10.1029/2022JC019479>
- BIPM. (2008). *Evaluation of measurement data—Guide to the expression of uncertainty in measurement*.
- Chau, T. T. T., Gehlen, M., & Chevallier, F. (2022). A seamless ensemble-based reconstruction of surface ocean CO₂ and air–sea CO₂ fluxes over the global coastal and open oceans. *Biogeosciences*, 19(4), 1087–1109. <https://doi.org/10.5194/bg-19-1087-2022>
- Demuth, H., Beale, M., & Hagan, M. (2008). *Neural Network Toolbox 6 Users Guide. The MathWorks, Inc.* 3 Apple Hill Drive, Natick, MA.
- Dong, Y., Yang, M., Bakker, D. C. E., Kitidis, V., & Bell, T. G. (2021). Uncertainties in eddy covariance air–sea CO₂ flux measurements and implications for gas transfer velocity parameterisations. *Atmospheric Chemistry and Physics*, 21(10), 8089–8110. <https://doi.org/10.5194/acp-21-8089-2021>
- Dong, Y., Bakker, D. C. E., Bell, T. G., Huang, B., Landschützer, P., Liss, P. S., & Yang, M. (2022). Update on the Temperature Corrections of Global Air-Sea CO₂ Flux Estimates. *Global Biogeochemical Cycles*, 36(9). <https://doi.org/10.1029/2022GB007360>

- Edson, J. B., Jampana, V., Weller, R. A., Bigorre, S. P., Plueddemann, A. J., Fairall, C. W., et al. (2013). On the Exchange of Momentum over the Open Ocean. *Journal of Physical Oceanography*, 43(8), 1589–1610. <https://doi.org/10.1175/JPO-D-12-0173.1>
- Fairall, C. W., Bradley, E. F., Godfrey, J. S., Wick, G. A., Edson, J. B., & Young, G. S. (1996). Cool-skin and warm-layer effects on sea surface temperature. *Journal of Geophysical Research: Oceans*, 101(C1), 1295–1308. <https://doi.org/10.1029/95JC03190>
- Fay, A. R., & McKinley, G. A. (2021). Observed Regional Fluxes to Constrain Modeled Estimates of the Ocean Carbon Sink. *Geophysical Research Letters*, 48(20), e2021GL095325. <https://doi.org/10.1029/2021GL095325>
- Fay, A. R., Gregor, L., Landschützer, P., McKinley, G. A., Gruber, N., Gehlen, M., et al. (2021). SeaFlux: harmonization of air–sea CO₂ fluxes from surface CO₂ data products using a standardized approach. *Earth System Science Data*, 13(10), 4693–4710. <https://doi.org/10.5194/essd-13-4693-2021>
- Ford, D. J., Tilstone, G. H., Shutler, J. D., Kitidis, V., Lobanova, P., Schwarz, J., et al. (2021). Wind speed and mesoscale features drive net autotrophy in the South Atlantic Ocean. *Remote Sensing of Environment*, 260, 112435. <https://doi.org/10.1016/j.rse.2021.112435>
- Ford, D. J., Tilstone, G. H., Shutler, J. D., & Kitidis, V. (2022a). Derivation of seawater pCO₂ from net community production identifies the South Atlantic Ocean as a CO₂ source. *Biogeosciences*, 19(1), 93–115. <https://doi.org/10.5194/bg-19-93-2022>
- Ford, D. J., Tilstone, G. H., Shutler, J. D., & Kitidis, V. (2022b). Identifying the biological control of the annual and multi-year variations in South Atlantic air–sea CO₂ flux. *Biogeosciences*, 19(17), 4287–4304. <https://doi.org/10.5194/bg-19-4287-2022>
- Ford, D. J., Sims, R. P., Shutler, J. D., Ashton, I., & Holding, T. (2023). Reanalysed (depth and temperature consistent) surface ocean CO₂ atlas (SOCAT) version 2023 (Version 2023-0) [Data set]. Zenodo. <https://doi.org/10.5281/ZENODO.8229316>
- Ford, D. J., Blannin, J., Watts, J., Watson, A. J., Landschutzer, P., Jersild, A., & Shutler, J. D. (2024). OceanICU Neural Network Framework with per pixel uncertainty propagation (Version v1.0.0). [Software]. <https://doi.org/10.5281/ZENODO.10868001>

- Friedlingstein, P., O’Sullivan, M., Jones, M. W., Andrew, R. M., Gregor, L., Hauck, J., et al. (2022). Global Carbon Budget 2022. *Earth System Science Data*, 14(11), 4811–4900.
<https://doi.org/10.5194/essd-14-4811-2022>
- Friedlingstein, P., O’Sullivan, M., Jones, M. W., Andrew, R. M., Bakker, D. C. E., Hauck, J., et al. (2023). Global Carbon Budget 2023. *Earth System Science Data*, 15(12), 5301–5369.
<https://doi.org/10.5194/essd-15-5301-2023>
- GEBCO Bathymetric Compilation Group. (2023). The GEBCO_2023 Grid - a continuous terrain model of the global oceans and land. (Version 1) [Documents, Network Common Data Form]. NERC EDS British Oceanographic Data Centre NOC. <https://doi.org/10.5285/F98B053B-0CBC-6C23-E053-6C86ABC0AF7B>
- Geilfus, N.-X., Tison, J.-L., Ackley, S. F., Galley, R. J., Rysgaard, S., Miller, L. A., & Delille, B. (2014). Sea ice CO₂ dynamics and air–ice CO₂ fluxes during the Sea Ice Mass Balance in the Antarctic (SIMBA) experiment – Bellingshausen Sea, Antarctica. *The Cryosphere*, 8(6), 2395–2407. <https://doi.org/10.5194/tc-8-2395-2014>
- Gloege, L., Yan, M., Zheng, T., & McKinley, G. A. (2022). Improved Quantification of Ocean Carbon Uptake by Using Machine Learning to Merge Global Models and pCO₂ Data. *Journal of Advances in Modeling Earth Systems*, 14(2), e2021MS002620.
<https://doi.org/10.1029/2021MS002620>
- Gregor, L., & Gruber, N. (2021). OceanSODA-ETHZ: a global gridded data set of the surface ocean carbonate system for seasonal to decadal studies of ocean acidification. *Earth System Science Data*, 13(2), 777–808. <https://doi.org/10.5194/essd-13-777-2021>
- Gregor, L., Lebehot, A. D., Kok, S., & Scheel Monteiro, P. M. (2019). A comparative assessment of the uncertainties of global surface ocean CO₂ estimates using a machine-learning ensemble (CSIR-ML6 version 2019a)-Have we hit the wall? *Geoscientific Model Development*, 12(12), 5113–5136. <https://doi.org/10.5194/gmd-12-5113-2019>
- Hauck, J., Landschützer, P., Mayot, N., & Jersild, A. (2023). Global Carbon Budget 2023, surface ocean fugacity of CO₂ (fCO₂) and air-sea CO₂ flux of individual global ocean biogeochemical

- models and surface ocean fCO₂-based data-products [Data set]. Zenodo.
<https://doi.org/10.5281/ZENODO.10222484>
- Hauck, J., Nissen, C., Landschützer, P., Rödenbeck, C., Bushinsky, S., & Olsen, A. (2023). Sparse observations induce large biases in estimates of the global ocean CO₂ sink: an ocean model subsampling experiment. *Philosophical Transactions of the Royal Society A: Mathematical, Physical and Engineering Sciences*, 381(2249), 20220063.
<https://doi.org/10.1098/rsta.2022.0063>
- Hersbach, H., Bell, B., Berrisford, P., Biavati, G., Horányi, A., Muñoz Sabater, J., Nicolas, J., et al. (2019). ERA5 monthly averaged data on single levels from 1979 to present. *Copernicus Climate Change Service (C3S) Climate Data Store (CDS) [Dataset]*.
<https://doi.org/10.24381/cds.fl7050d7>
- Ho, D. T., Wanninkhof, R., Schlosser, P., Ullman, D. S., Hebert, D., & Sullivan, K. F. (2011). Toward a universal relationship between wind speed and gas exchange: Gas transfer velocities measured with ³He/SF₆ during the Southern Ocean Gas Exchange Experiment. *Journal of Geophysical Research*, 116, C00F04. <https://doi.org/10.1029/2010JC006854>
- Holding, T., Ashton, I. G., Shutler, J. D., Land, P. E., Nightingale, P. D., Rees, A. P., et al. (2019). The FluxEngine air–sea gas flux toolbox: simplified interface and extensions for in situ analyses and multiple sparingly soluble gases. *Ocean Science*, 15(6), 1707–1728.
<https://doi.org/10.5194/os-15-1707-2019>
- Iida, Y., Takatani, Y., Kojima, A., & Ishii, M. (2021). Global trends of ocean CO₂ sink and ocean acidification: an observation-based reconstruction of surface ocean inorganic carbon variables. *Journal of Oceanography*, 77(2), 323–358. <https://doi.org/10.1007/s10872-020-00571-5>
- Jean-Michel, L., Eric, G., Romain, B.-B., Gilles, G., Angélique, M., Marie, D., et al. (2021). The Copernicus Global 1/12° Oceanic and Sea Ice GLORYS12 Reanalysis. *Frontiers in Earth Science*, 9(July), 1–27. <https://doi.org/10.3389/feart.2021.698876>

- Jersild, A., & Landschützer, P. (2024). A Spatially Explicit Uncertainty Analysis of the Air-Sea CO₂ Flux From Observations. *Geophysical Research Letters*, 51(4), e2023GL106636.
<https://doi.org/10.1029/2023GL106636>
- Kern, S. (2021). Spatial Correlation Length Scales of Sea-Ice Concentration Errors for High-Concentration Pack Ice. *Remote Sensing*, 13(21), 4421. <https://doi.org/10.3390/rs13214421>
- Kohout, A. L., & Meylan, M. H. (2008). An elastic plate model for wave attenuation and ice floe breaking in the marginal ice zone. *Journal of Geophysical Research: Oceans*, 113(C9), 2007JC004434. <https://doi.org/10.1029/2007JC004434>
- Lan, X., Tans, P., Thoning, K., & NOAA Global Monitoring Laboratory. (2023). NOAA Greenhouse Gas Marine Boundary Layer Reference - CO₂. [Data set]. NOAA GML.
<https://doi.org/10.15138/DVNP-F961>
- Landschützer, P., Gruber, N., Bakker, D. C. E., Schuster, U., Nakaoka, S., Payne, M. R., et al. (2013). A neural network-based estimate of the seasonal to inter-annual variability of the Atlantic Ocean carbon sink. *Biogeosciences*, 10(11), 7793–7815. <https://doi.org/10.5194/bg-10-7793-2013>
- Landschützer, P., Gruber, N., Bakker, D. C. E., & Schuster, U. (2014). Recent variability of the global ocean carbon sink. *Global Biogeochemical Cycles*, 28(9), 927–949.
<https://doi.org/10.1002/2014GB004853>
- Landschützer, P., Gruber, N., & Bakker, D. C. E. (2016). Decadal variations and trends of the global ocean carbon sink. *Global Biogeochemical Cycles*, 30(10), 1396–1417.
<https://doi.org/10.1002/2015GB005359>
- Landschützer, P., Gruber, N., Bakker, D. C. E., Stemmler, I., & Six, K. D. (2018). Strengthening seasonal marine CO₂ variations due to increasing atmospheric CO₂. *Nature Climate Change*, 8(2), 146–150. <https://doi.org/10.1038/s41558-017-0057-x>
- Leighton, T. G., Coles, D. G. H., Srokosz, M., White, P. R., & Woolf, D. K. (2018). Asymmetric transfer of CO₂ across a broken sea surface. *Scientific Reports*, 8(1), 8301.
<https://doi.org/10.1038/s41598-018-25818-6>
- Longhurst, A. (1998). *Ecological geography of the sea*. San Diego: Academic Press.

- Mälicke, M. (2022). SciKit-GStat 1.0: a SciPy-flavored geostatistical variogram estimation toolbox written in Python. *Geoscientific Model Development*, 15(6), 2505–2532.
<https://doi.org/10.5194/gmd-15-2505-2022>
- Mears, C., Lee, T., Ricciardulli, L., Wang, X., & Wentz, F. (2022a). Improving the Accuracy of the Cross-Calibrated Multi-Platform (CCMP) Ocean Vector Winds. *Remote Sensing*, 14(17), 4230. <https://doi.org/10.3390/rs14174230>
- Mears, C., Lee, T., Ricciardulli, L., Wang, X., & Wentz, F. (2022b). RSS Cross-Calibrated Multi-Platform (CCMP) monthly ocean vector wind analysis on 0.25 deg grid, Version 3.0 [Data set]. <https://doi.org/10.56236/RSS-uv1m30>
- Merchant, C. J., Embury, O., Bulgin, C. E., Block, T., Corlett, G. K., Fiedler, E., et al. (2019). Satellite-based time-series of sea-surface temperature since 1981 for climate applications. *Scientific Data*, 6(1), 223. <https://doi.org/10.1038/s41597-019-0236-x>
- Nightingale, P. D., Malin, G., Law, C. S., Watson, A. J., Liss, P. S., Liddicoat, M. I., et al. (2000). In situ evaluation of air-sea gas exchange parameterizations using novel conservative and volatile tracers. *Global Biogeochemical Cycles*, 14(1), 373–387.
<https://doi.org/10.1029/1999GB900091>
- OSI SAF. (2022). GBL SICO CDR R3Global Sea Ice Concentration Climate Data Record v3.0 - Multimission (Version 3) [netCDF4]. OSI SAF.
https://doi.org/10.15770/EUM_SAF_OSI_0013
- Prytherch, J., & Yelland, M. J. (2021). Wind, Convection and Fetch Dependence of Gas Transfer Velocity in an Arctic Sea-Ice Lead Determined From Eddy Covariance CO₂ Flux Measurements. *Global Biogeochemical Cycles*, 35(2), e2020GB006633.
<https://doi.org/10.1029/2020GB006633>
- Regnier, P., Resplandy, L., Najjar, R. G., & Ciais, P. (2022). The land-to-ocean loops of the global carbon cycle. *Nature*, 603(7901), 401–410. <https://doi.org/10.1038/s41586-021-04339-9>
- Roobaert, A., Laruelle, G. G., Landschützer, P., & Regnier, P. (2018). Uncertainty in the global oceanic CO₂ uptake induced by wind forcing: quantification and spatial analysis. *Biogeosciences*, 15(6), 1701–1720. <https://doi.org/10.5194/bg-15-1701-2018>

- Shutler, J. D., Land, P. E., Piolle, J. F., Woolf, D. K., Goddijn-Murphy, L., Paul, F., et al. (2016).
FluxEngine: A flexible processing system for calculating atmosphere-ocean carbon dioxide
gas fluxes and climatologies. *Journal of Atmospheric and Oceanic Technology*, 33(4), 741–
756. <https://doi.org/10.1175/JTECH-D-14-00204.1>
- Shutler, J. D., Wanninkhof, R., Nightingale, P. D., Woolf, D. K., Bakker, D. C., Watson, A., et al.
(2020). Satellites will address critical science priorities for quantifying ocean carbon.
Frontiers in Ecology and the Environment, 18(1), 27–35. <https://doi.org/10.1002/fee.2129>
- Shutler, J. D., Gruber, N., Findlay, H. S., Land, P. E., Gregor, L., Holding, T., et al. (2024). The
increasing importance of satellite observations to assess the ocean carbon sink and ocean
acidification. *Earth-Science Reviews*, 250, 104682.
<https://doi.org/10.1016/j.earscirev.2024.104682>
- Takahashi, T., Sutherland, S. C., Wanninkhof, R., Sweeney, C., Feely, R. A., Chipman, D. W., et al.
(2009). Climatological mean and decadal change in surface ocean pCO₂, and net sea-air CO₂
flux over the global oceans. *Deep-Sea Research Part II: Topical Studies in Oceanography*,
56(8–10), 554–577. <https://doi.org/10.1016/j.dsr2.2008.12.009>
- Taylor, J. R. (1997). *An introduction to error analysis*. Sausalito, Calif.: University Science Books.
- Wanninkhof, R. (2014). Relationship between wind speed and gas exchange over the ocean revisited.
Limnology and Oceanography: Methods, 12(JUN), 351–362.
<https://doi.org/10.4319/lom.2014.12.351>
- Wanninkhof, R., Park, G. H., Takahashi, T., Sweeney, C., Feely, R., Nojiri, Y., et al. (2013). Global
ocean carbon uptake: Magnitude, variability and trends. *Biogeosciences*, 10(3), 1983–2000.
<https://doi.org/10.5194/bg-10-1983-2013>
- Watson, A. J., Schuster, U., Bakker, D. C. E., Bates, N. R., Corbière, A., González-Dávila, M., et al.
(2009). Tracking the Variable North Atlantic Sink for Atmospheric CO₂. *Science*, 326(5958),
1391–1393. <https://doi.org/10.1126/science.1177394>
- Watson, A. J., Schuster, U., Shutler, J. D., Holding, T., Ashton, I. G. C., Landschützer, P., et al. (2020).
Revised estimates of ocean-atmosphere CO₂ flux are consistent with ocean carbon inventory.
Nature Communications, 11(1), 1–6. <https://doi.org/10.1038/s41467-020-18203-3>

- Watts, J., Bell, T. G., Anderson, K., Butterworth, B. J., Miller, S., Else, B., & Shutler, J. (2022). Impact of sea ice on air-sea CO₂ exchange – A critical review of polar eddy covariance studies. *Progress in Oceanography*, 201, 102741. <https://doi.org/10.1016/j.pocean.2022.102741>
 - Weiss, R. F. (1974). Carbon dioxide in water and seawater: the solubility of a non-ideal gas. *Marine Chemistry*, 2(3), 203–215. [https://doi.org/10.1016/0304-4203\(74\)90015-2](https://doi.org/10.1016/0304-4203(74)90015-2)
 - Weiss, R. F., & Price, B. A. (1980). Nitrous oxide solubility in water and seawater. *Marine Chemistry*, 8(4), 347–359. [https://doi.org/10.1016/0304-4203\(80\)90024-9](https://doi.org/10.1016/0304-4203(80)90024-9)
 - Woolf, D. K., Land, P. E., Shutler, J. D., Goddijn-Murphy, L. M., & Donlon, C. J. (2016). On the calculation of air-sea fluxes of CO₂ in the presence of temperature and salinity gradients. *Journal of Geophysical Research: Oceans*, 121(2), 1229–1248. <https://doi.org/10.1002/2015JC011427>
 - Woolf, D. K., Shutler, J. D., Goddijn-Murphy, L., Watson, A. J., Chapron, B., Nightingale, P. D., et al. (2019). Key Uncertainties in the Recent Air-Sea Flux of CO₂. *Global Biogeochemical Cycles*, 33(12), 1548–1563. <https://doi.org/10.1029/2018GB006041>
- References from Supporting Information**
- CMEMS. (2021). Copernicus Marine Modelling Service global ocean physics reanalysis product (GLORYS12V1). Copernicus Marine Modelling Service [Data Set]. <https://doi.org/10.48670/moi-00021>
 - Ford, D. J., Sims, R. P., Shutler, J. D., Ashton, I., & Holding, T. (2023). Reanalysed (depth and temperature consistent) surface ocean CO₂ atlas (SOCAT) version 2023 (Version 2023-0) [Data set]. Zenodo. <https://doi.org/10.5281/ZENODO.8229316>
 - Hauck, J., Landschützer, P., Mayot, N., & Jersild, A. (2023). Global Carbon Budget 2023, surface ocean fugacity of CO₂ (fCO₂) and air-sea CO₂ flux of individual global ocean biogeochemical models and surface ocean fCO₂-based data-products [Data set]. Zenodo. <https://doi.org/10.5281/ZENODO.10222484>
 - Hersbach, H., Bell, B., Berrisford, P., Biavati, G., Horányi, A., Muñoz Sabater, J., Nicolas, J., et al. (2019). ERA5 monthly averaged data on single levels from 1979 to present. Copernicus Climate Change Service (C3S) Climate Data Store (CDS) [Dataset]. <https://doi.org/10.24381/cds.fl7050d7>

- 948 Jean-Michel, L., Eric, G., Romain, B.-B., Gilles, G., Angélique, M., Marie, D., et al. (2021). The
949 Copernicus Global 1/12° Oceanic and Sea Ice GLORYS12 Reanalysis. *Frontiers in Earth Science*,
950 9(July), 1–27. <https://doi.org/10.3389/feart.2021.698876>
- 951 Lan, X., Tans, P., Thoning, K., & NOAA Global Monitoring Laboratory. (2023). NOAA Greenhouse
952 Gas Marine Boundary Layer Reference - CO₂. [Data set]. NOAA GML.
953 <https://doi.org/10.15138/DVNP-F961>
- 954 Mears, C., Lee, T., Ricciardulli, L., Wang, X., & Wentz, F. (2022a). Improving the Accuracy of the
955 Cross-Calibrated Multi-Platform (CCMP) Ocean Vector Winds. *Remote Sensing*, 14(17), 4230.
956 <https://doi.org/10.3390/rs14174230>
- 957 Mears, C., Lee, T., Ricciardulli, L., Wang, X., & Wentz, F. (2022b). RSS Cross-Calibrated Multi-
958 Platform (CCMP) monthly ocean vector wind analysis on 0.25 deg grid, Version 3.0 [Data set].
959 <https://doi.org/10.56236/RSS-uv1m30>
- 960 Merchant, C. J., Embury, O., Bulgin, C. E., Block, T., Corlett, G. K., Fiedler, E., et al. (2019).
961 Satellite-based time-series of sea-surface temperature since 1981 for climate applications. *Scientific*
962 *Data*, 6(1), 223. <https://doi.org/10.1038/s41597-019-0236-x>
- 963 Taylor, J. R. (1997). *An introduction to error analysis*. Sausalito, Calif.: University Science Books.
- 964